JOURNAL OF MATERIALS SCIENCE 38 (2003) 4145–4155

Surface topography evolution and fatigue fracture of polysilicon

S. M. ALLAMEH, P. SHROTRIYA
Department of Mechanical and Aerospace Engineering, The Princeton Materials Institute, Princeton, NJ 08544, USA
A. BUTTERWICK
Department of Engineering Physics, University of Michigan, Ann Arbor, MI 48105, USA
S. BROWN
Exponent Failure Analysis, Natick, MA 01760, USA
NAN YAO, W. SOBOYEJO
Department of Mechanical and Aerospace Engineering, The Princeton Materials Institute, Princeton, NJ 08544, USA

This paper presents the results of an experimental stydy of the micromechanisms of fatigue crack nucleation and fatigue fracture in polysilicon MEMS Structures. The initial stages of fatigue are shown to be associated with stress-assisted surface topography evolution and the thickening of SiO_2 layers that form on the unpassivated polysilicon surfaces and crack/notch faces. The differences in surface topography and oxide thickness are elucidated as functions of fatigue cycling before discussing the micromechanisms of crack growth and final fracture. © *2003 Kluwer Academic Publishers*

1. Introduction

There is increasing interest in the miniaturization of devices in a wide range of applications. This is due largely to the significant improvement in portability, cost and effectiveness of microelectromechanical systems (MEMS) devices, combined with their enhanced functionality and fast response time [1, 2]. This has lead to a tremendous growth of MEMS market [1]. Typical MEMS devices include any combination of microsensors and microactuators. They may also include the logic units that condition the signals from the sensors, make a decision, and actuate mechanical microactuators. Accelerometers, drug delivery systems, lab-on-a-chip systems and optical switches are just a few examples of emerging MEMS structures.

Despite the extensive research on the design and characterization of various properties of MEMS structures, there is still a need for the development of MEMS reliability models [3]. In cyclically actuated Si MEMS structures, mechanism-based reliability models are needed for the prediction of fatigue life [1]. However, unlike bulk materials in which the growth component dominates the fatigue life, the micron-scale sizes of MEMS structures are in a regime where the initiation component of the total fatigue life becomes important. This study will, therefore, focus on the phenomena associated largely with fatigue crack initiation. However, some discussion on crack growth and final fracture mechanisms will also be presented during the latter stages of the paper.

Since most of the MEMS devices in service are fabricated from polysilicon [1], the current study will examine the fatigue behavior of polysilicon. Silicon is the material of choice due to its high strength (1-4.3 GPa) [4–6] and ease of fabrication with techniques developed originally for semi-conductor manufacturing [2]. However, Si also has a relatively low fracture toughness (~ 1 MPa$\sqrt{\text{m}}$ [7–11]. Furthermore, in bulk form, silicon is not expected to exhibit conventional brittle or ductile fatigue [12, 13]. Nevertheless, it is well established that polysilicon undergoes fatigue damage under ambient conditions [5, 7, 14–18]. Water and water vapor are also known to accelerate fatigue processes in Si MEMS structures leading ultimately to premature fracture of polysilicon components [5].

Prior work on the surface morphology evolution of solids have resulted in a number of models that may be used to develop insights into the effects of environment on fatigue behavior of polysilicon. These include: the energy-based model of Yang and Srolovitz [19] and the interface reaction/activation volume arguments of Liang and Suo [20]. The first model relates the surface morphology evolution of a stressed solid to the kinetic mechanism of materials transport. It predicts that surface instability creates a groove that sharpens, as it grows deeper and the growth rate accelerates until crack acquires a critical length [19]. In the second approach, the dissolution rate of a stressed surface exposed to aggressive environments is related not only to the driving force, but also to the activation energy of the reaction taking place on the surface [20]. The current work explores the above arguments within a combined experimental and analytical framework.

This paper examines the material changes that lead ultimately to the crack nucleation and growth in unpassivated polysilicon MEMS structures. The initiation

stage is associated with surface topography evolution and surface oxidation. It is presumed that the observed surface micro-groove evolution leads ultimately to micro-crack nucleation in the topical SiO_2 layer. The mechanisms of notch-tip deformation and fast fracture under cyclic loading are elucidated, respectively, using transmission electron microscopy (TEM), and atomic force microscopy (AFM). The implications of the results are then discussed for the development of mechanism-based fatigue crack initiation models.

2. Material

The polysilicon MEMS structures that were used in this study were cantilevers with one end fixed, and the other connected to an interdigitating, capacitively driven comb drive (Fig. 1).

They were fabricated in batch runs at JDS Uniphase (formerly MCNC or Cronos Integrated Microsystems) of Raleigh-Durham, NC. Details of fabrication process can be found in [2]. The gauge section of the cantilevers had dimensions of 10 μm × 10 μm, with a thickness of 2 μm. They were notched with the narrow section of the cantilever, being 5 mm directly beneath the notch. Fig. 2 shows a scanning electron microscopy (SEM) image of a notched sample. The image reveals a nano-scale structure with an average grain size of about 200 nm (Fig. 2).

3. Experimental procedure

The polysilicon MEMS structures were sealed by a topical SiO_2 layer in the as-received condition. To measure the angular displacement of the cantilever, micrographs obtained from optical microscope were analyzed. The details of microvision techniques that were used for the displacement measurements are shown in Fig. 3. An ultra bright green light emitting diode (LED) was powered at a frequency slightly less than that of the device. This allowed the device to be observed with a slow motion that was recorded and analyzed frame-by-frame using an image analysis software package obtained from National Instruments, Austin, TX. The magnitude of angular displacement was obtained from the amplitude of a sine wave curve, fitted to the displacement versus time graph. The angular displacement was found to be linearly proportional to the square of actuation voltage. The resulting calibration curve obtained for a range of actuation voltages between 35 and 145 V is presented in Fig. 4.

The polysilicon resonating structures were released by a 5-min soak in 49.6% HF, followed by a 10-min soak in water and a 10-min soak in methanol. The samples were dried in air by placing them on a hot plate with a surface temperature of 110°C for 2 min. Gold wire bonding was performed to connect the contact pads of the devices to an edge connector.

Details of the actuation of the sample are shown schematically in Fig. 3. The actuation of the samples was performed in ambient air (75% relative humidity) using an alternating current (AC) signal from a Hewlett-Packard wave function generator and amplified by an APEX amplifier to levels between 0–250 V. The frequency of the drive was chosen such that it would synchronize with the first harmonic of the devices (∼40.9 kHz for the notched samples). This was verified experimentally by imaging the device oscillating in one direction with a strobe light frequency of 40.2 kHz. Upon doubling of the strobe frequency, the resulting double images revealed the bi-directional motion of the device, as expected at such a frequency.

An *in situ* atomic force microscope was used to study the evolution of surface topography at the bottom of the notch, where, the stresses are relatively high. Tapping mode AFM allowed imaging of surface during actuation. Continuous recording of images allowed quantitative measurement of the extent of change in surface topography with the number of fatigue cycles.

In order to study the microstructural changes due to deformation at the notch tip, TEM foils were prepared using focused ion beam microscopy (FIB). These foils were prepared from actuated and unactuated samples to compare the two microstructures. A dual beam FIB FEI Strata TM DB 235 microscope was used to slice the specimens right at the bottom of the notch. The width of the slice was in the longitudinal direction of the specimen, perpendicular to the notch axis. The slices were made using a gallium ion beam operated at 30 kV. The foils, still attached by platinum ligaments, were ion-milled to electron transparency before completely detaching them from the specimens. The foils were then placed on a TEM grid covered with a topical carbon film and moved to TEM. A Phillips CM-200 transmission electron microscope operated at 200 kV was used to study the microstructure of the foils. This

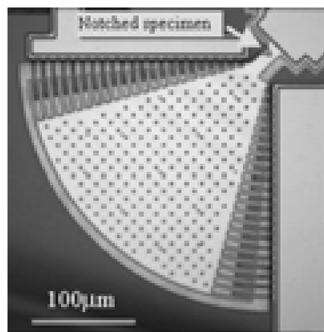

Figure 1 Capacitively driven comb drive test structure.

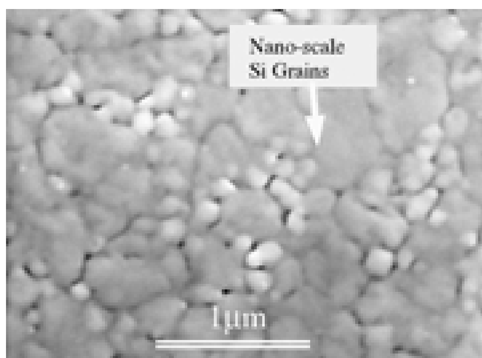

Figure 2 High magnification secondary electron image of the surface showing nano-scale grains.

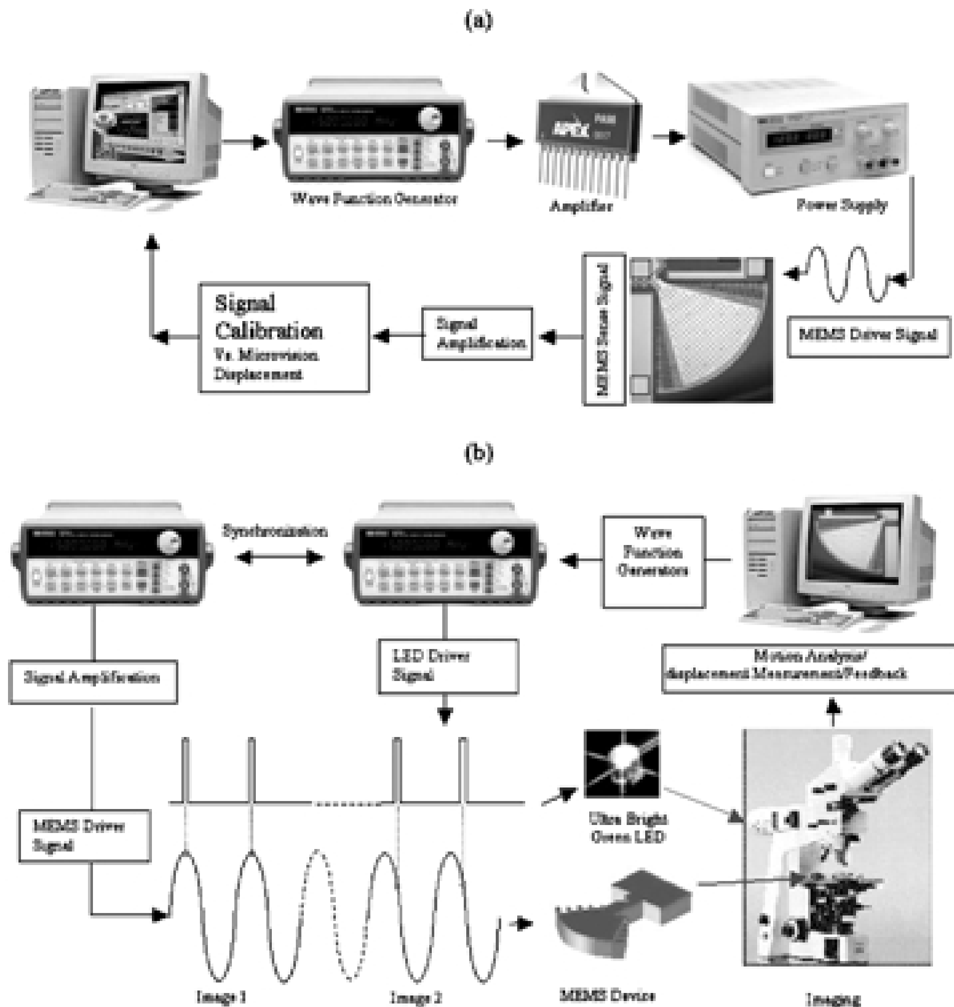

Figure 3 Schematic representation of (a) actuation process for polysilicon MEMS structures and (b) micro-vision system for the detection of the range of motion of the device and calibration of the angular displacement versus the actuation voltage.

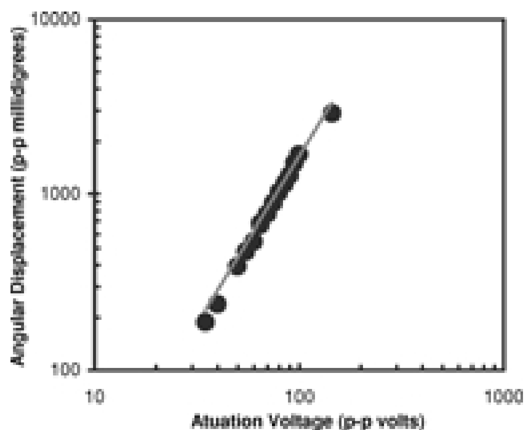

Figure 4 Calibration curve obtained by using the *in situ* micro-vision system on polysilicon structures actuated at voltages between 35–130 V.

included grain size, shape and orientation, and dislocation substructures in foils obtained from actuated and unactuated specimens.

4. Results and discussion

4.1. Surface topography evolution

Typical scanned images obtained from in-situ AFM are presented in Fig. 5a–d. The surface of the unactuated sample is imaged on a 2 μm $\times$ 2 μm scale in Fig. 5a. A corresponding image obtained after actuation is presented in Fig. 5b. Similar images covering larger areas under the notch are presented on a 5 μm x 5 μm scale in Fig. 5c and 5d for the unactuated and actuated surfaces respectively. The change in the surface topography is quite evident from these images. The arrows show the location of the bottom of the notch on the 3-D images.

It is clear from Fig. 5a–d that the extent of the change in surface topography is large for areas in the immediate vicinity of the bottom of the notch. However, the change is minimal in the areas away from the notch. This clearly establishes a strong correlation between the level of stress and the extent of change in topography. A comparison between Fig. 5a and 5b shows that smaller-size features in the areas close to the notch are diminished, while a large depression has developed in their place. On a larger scale, Fig. 5c–d show the extent of the change over a larger area.

To quantify the extent of change in the topography of the sample as a function of distance from the bottom of the notch, which is an indication of stress level, image subtraction was used. Fig. 6 shows two AFM images 6a before and 6b after actuation for 12.79×10^9 cycles. Fig. 6c is the subtracted image that shows the extent of change in the surface topography during actuation. Areas that are pink or orange have undergone the highest

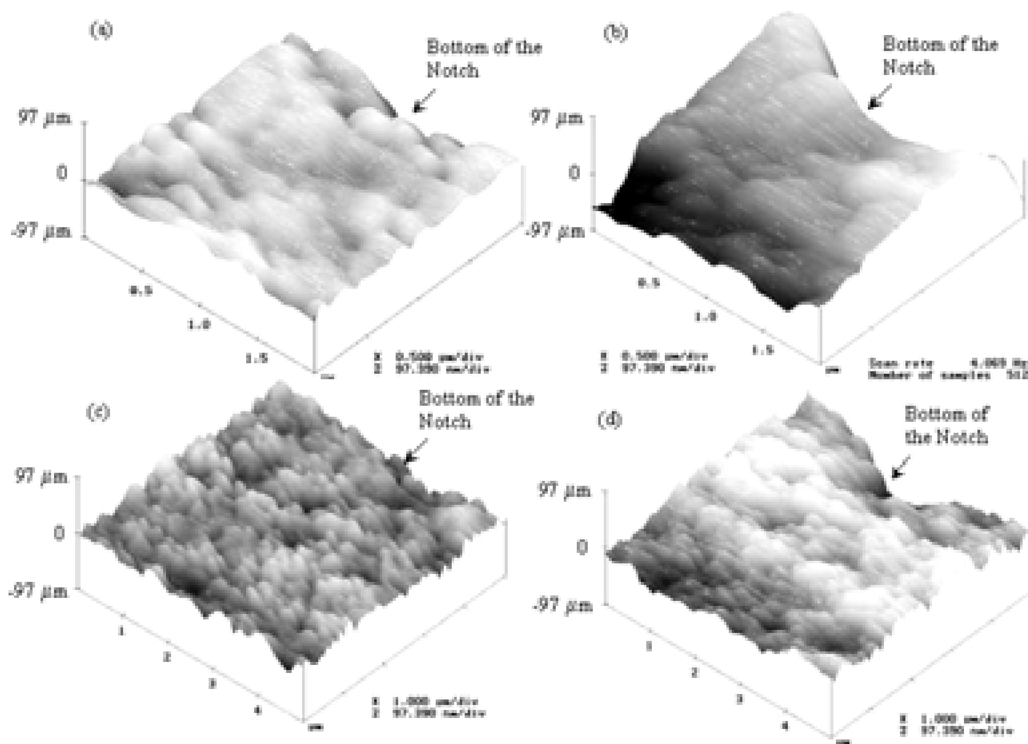

Figure 5 Surface topography evolution showing in a series of AFM surface scans of the area below the notch tip: (a) Before actuation, (b) After the actuation of polysilicon structures for 2×10^9 cycles on a 2 μm × 2 μm scale; (c) and (d) are corresponding images on a 5 μm × 5 μm scale (before and after actuation, respectively).

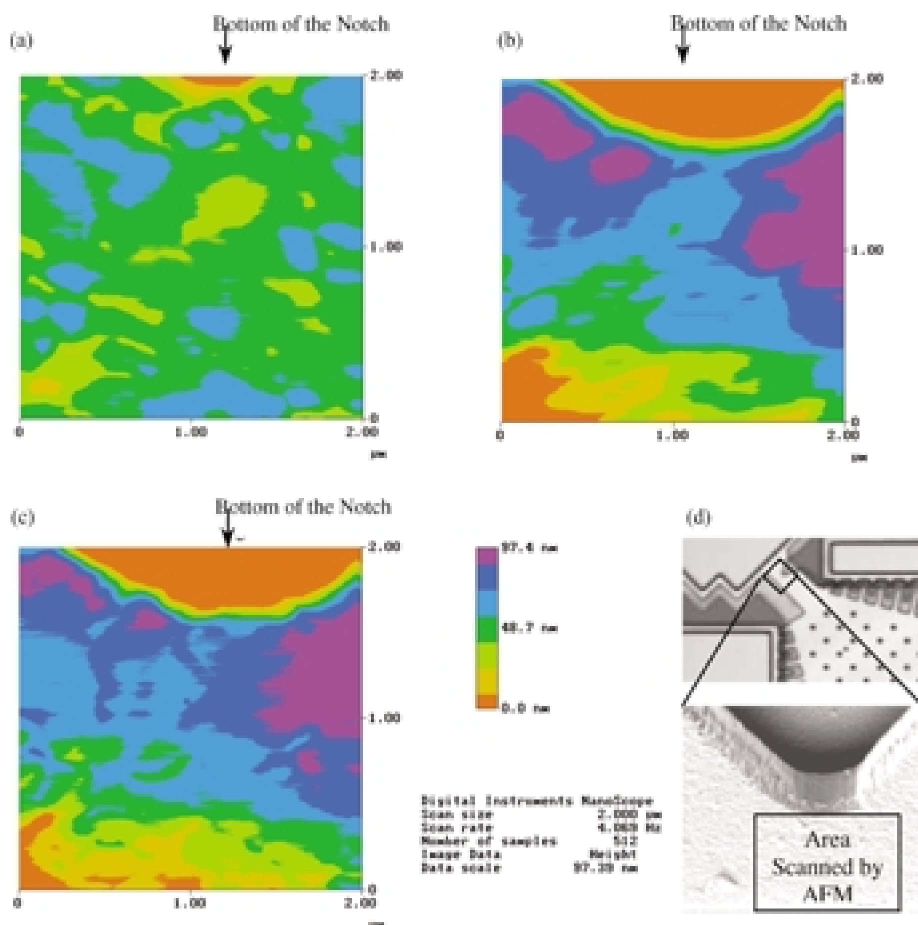

Figure 6 Quantitative analysis of the extent of change in the surface topography during actuation of polysilicon structures by image subtraction: (a) Before actuation, (b) After 12.79×10^9 cycles, (c) Image subtraction, and (d) Photographs showing area scanned by AFM in the vicinity of the notch.

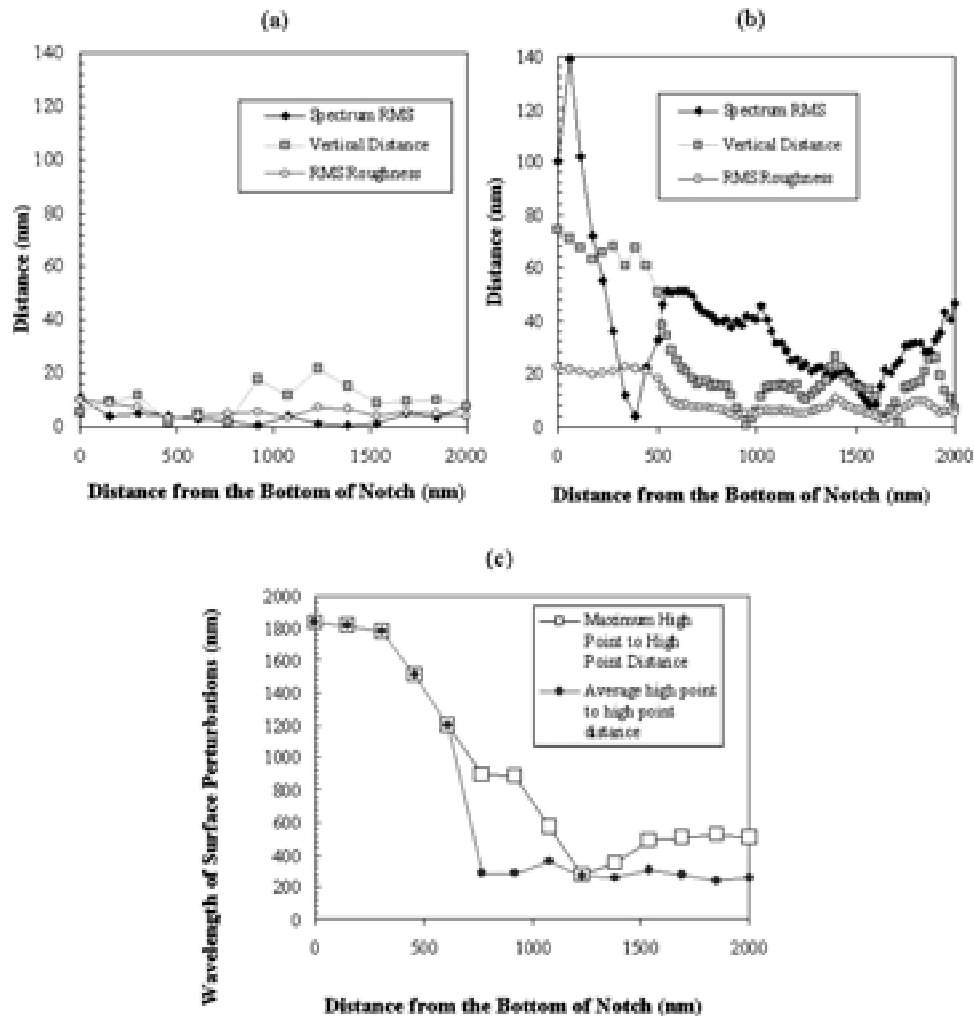

Figure 7 Amplitude and wavelength evolution during the cyclic actuation of polysilicon structures. These show effects in the areas at the bottom of the notch. Roughness parameters plotted against the distance from the bottom of the notch: (a) Before actuation, (b) After 2×10^9 cycles, and (c) Wavelength of surface perturbations plotted against the distance from the bottom of the notch.

degree of change. As expected, these areas are mostly concentrated at the bottom of the notch.

The topography evolution can also be evaluated using roughness information from the scan lines taken progressively from the surface of the sample at regular intervals. Fig. 7a and 7b show the root-mean square (RMS) roughness values of the surface before and after actuation, respectively. The RMS roughness does not change significantly with distance from the bottom of the notch for the unactuated sample. However, for the actuated surface, the RMS roughness is much higher in regions that were closer to the bottom of the notch (Fig. 7b).

The information extracted from the scan profiles also shows the changes in the wavelength and amplitudes of the surface perturbations during actuation. The increase in the amplitude of surface perturbations, close to the notch, can be observed by comparing Fig. 7a with Fig. 7b. While the amplitudes are relatively uniform across the sample in the direction of the notch-axis for the unactuated surface (Fig. 7a), the amplitudes are much higher at the bottom of the notch in the actuated sample (Fig. 7b). The corresponding wavelength of the perturbations also increases upon actuation in the areas close to the bottom of the notch. Fig. 7c shows a 6-fold increase in the average wavelength (expressed in terms of average high point to high point) in the areas at the bottom of the notch.

4.2. Finite element analysis

To evaluate the magnitude, type and distribution of stresses, finite element analyses (FEA) were performed. Fig. 8a shows the mesh that was used for the calculations. Details of finite element analyses are presented elsewhere [21]. Mesh refinement was carried out until the elastic energy converged. In the calculations, Young's Modulus was taken as 169 GPa [22]. The spatial distribution of stress in a 5-micron wide slice of the sample around the notch is shown in Fig. 8b.

The highest magnitude of stress was associated with an area in the near vicinity of the notch root. This had a value of 2.76 GPa. Regions away from the notch, (at the other edge across the sample) had stress levels that were much lower than those at the notch root (due to the lack of stress concentrators) but with an opposite sign. The maximum stress generated in this region was 201 MPa. Calculations were performed, not only for the sample, but also for the whole suspended mass, including the drive structure. The concentration of high stresses at the notch root is consistent with the highest extent of surface topography evolution in this area.

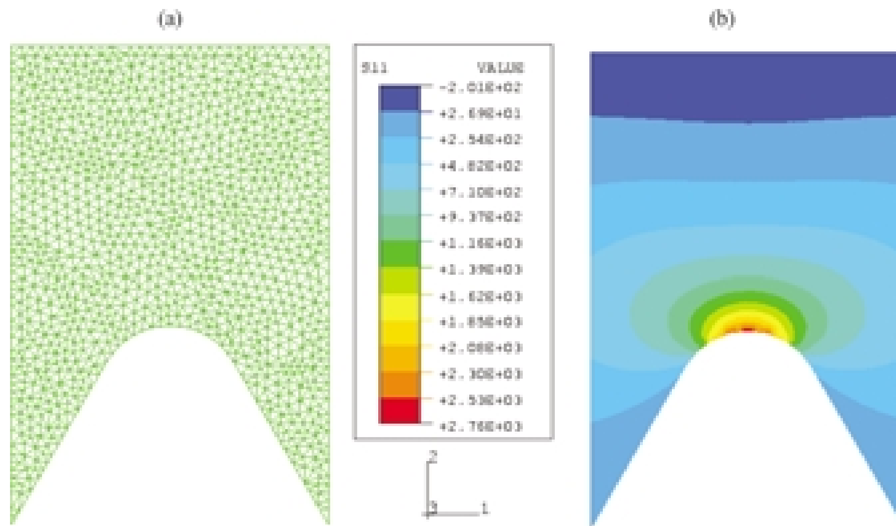

Figure 8 Spatial stress distribution in the notch region of the cantilever along with the mesh used to calculate the stress magnitude.

4.3. Linear perturbation analysis

The influence of the changes in surface topography evolution on crack initiation was studied by linear perturbation analysis. Details of this analysis is given in [21]. Scan lines obtained from a location on the sample during actuation is analyzed in this analysis. These scan lines were extracted from the pictures recorded during continuous imaging of the surface. The pictures were corrected for possible translations or rotations of the sample during actuation. The corrections were accomplished by a special program that matches the landmarks of any two consecutive images. Scan lines obtained from three locations on the surface of the sample with 0.2, 0.8, and 1.8 μm from the bottom of the notch are shown in a focused ion beam (FIB) image of the sample (Fig. 9). Fig. 9a is a FIB image of the surface of the sample marked by the scan lines. Fig. 9b–d show the change in the profiles of the scan lines with the evolution of surface topography.

Scan lines obtained from the area close to the notch root are presented in Fig. 9b. The bottom most profile is extracted from the 16th image (early stages, 9.2×10^3seconds into actuation). On the other hand, The topmost profile, represents the topography in the later stages. This scan line was extracted from the 380th image (late stages, 2.14×10^4 s into actuation). Scan lines obtained from intermediate stages of actuation are also shown in the diagram. These include those extracted

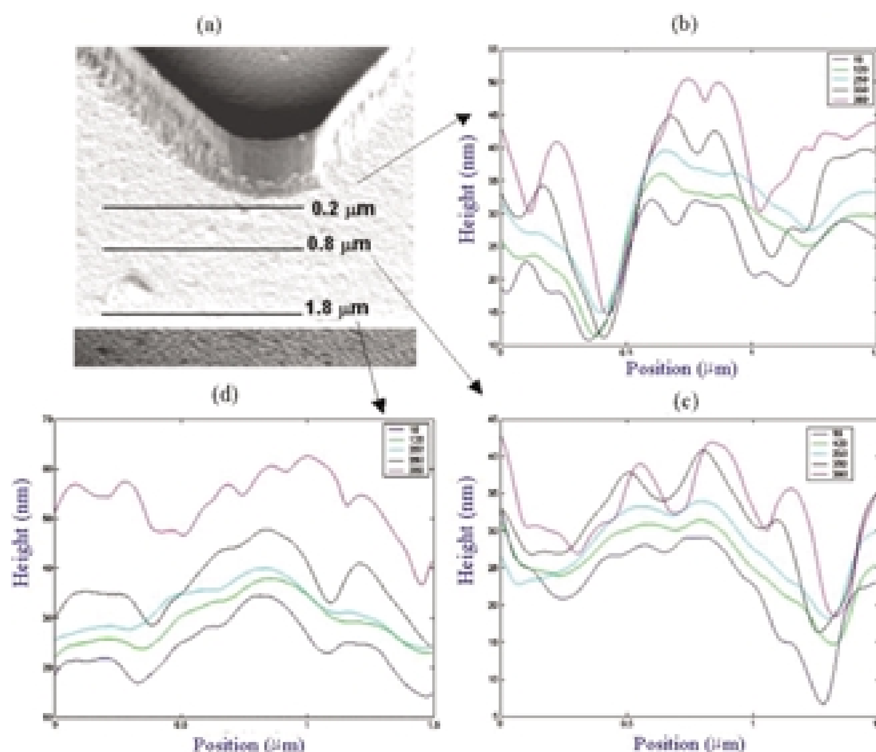

Figure 9 Linear perturbation analysis versus cycles and position (a) Location of the three scan lines (b–d). Scan profiles taken at various stages of actuation with distances from the bottom of the notch of 0.2 μm 0.8 μm and 1.8 μm, respectively.

from the 120th, 250th and 350th images (1.47×10^4, 1.67×10^4, 1.99×10^4 s into actuation respectively). This scan line was of the highest stress level compared to the other two locations. The maximum stress level associated with this location was about 2.6 GPa. Because this scan line is in the proximity of the notch root, it is expected to have the highest degree of surface topography evolution compared to the other two locations. Fig. 9b clearly shows significant deepening of the grooves, which is the evidence for a high degree of topography change, associated with this scan line.

Scan lines obtained from the area far away (1.8 μm) from the notch root are presented in Fig. 9d. In contrast to the area close to the notch root, the depth of the grooves did not change significantly. This is consistent with a significantly smaller stress level of about 700 MPa for this location. The third set of scan lines obtained from an area in an intermediate region (0.8 μm away from the notch root) are shown in Fig. 9c. Consistent with the stress level at this location (1.6 GPa), these scan lines show some deepening of the grooves, which manifests a moderate change in surface topography.

The perturbation technique used here was developed initially by Mullins (1957) [23], and later expanded by Yang and Srolovitz [19], Srolovitz [24], and Yu and Suo [25]. Surface of a stressed solid is considered to be unstable with respect to perturbation of sufficiently large wavelength. For the case of stressed polysilicon surfaces exposed to water or water vapor, topography evolution is attributed to stress-assisted dissolution of the SiO_2 layer on top of silicon. Time evolution of a Fourier component, $q(\omega, t)$ of the surface roughness can be related to principal stresses through the parameter α as follows (Kim *et al.*, 1999) [26] and (Yu and Suo, 2000) [25].

$$\ln \frac{q(\omega, t)}{q(\omega, 0)} = M\alpha t \tag{1}$$

$$\alpha = \frac{2(1+\nu)}{E}\left[(1-\nu)\left(\sigma_1 \cos^2\theta + \sigma_2 \sin^2\theta\right)^2 + (\sigma_1 - \sigma_2)^2 \cos^2\theta \sin^2\theta\right]\omega - \gamma\omega^2 \tag{2}$$

From Equation 1, it is clear that the amplitude of Fourier component grows if $\alpha > 0$ and decays if $\alpha < 0$. To calculate α, the root mean square average of the cyclic stresses near the notch root was used. In order to identify the Fourier components with amplitudes that grow with time, fast Fourier transforms of the surface morphologies (before and after actuation) were obtained according to Equation 2. In this manner, Fig. 10b was constructed to help determine the mechanism governing the topography evolution in polysilicon during actuation in ambient air.

A comparison between α plots (Fig. 10a) and the map that shows the changes of wave vectors (Fig. 10b) has been made in Fig. 10. This shows that the two diagrams have similar characteristics. The strong similarities support the model that attributes surface morphology evolution to stress-assisted dissolution of SiO_2 layer.

Details of microgroove deepening with time were shown in scan lines presented in Fig. 9. Curve fitting the data obtained from these scan lines produced curves presented in Fig. 11. Amplitude of the grooves is clearly seen to increase with actuation time. The largest increase is associated with the scan line in the proximity of the notch root where local stresses are highest compared to the locations away from the notch.

4.4. Notch-root deformation

Fig. 12 shows the results of TEM analyses of the notch-tip regions in the polysilicon structure subjected to cyclic fatigue loading. A slice of the cantilever at the location of the notch, parallel to the axis of the notch, but perpendicular to the bottom of the notch, was prepared with a dual-beam focused ion beam (FIB), as shown in Fig. 12a. The microstructure of the unactuated sample is presented in the secondary electron (SE) image of Fig. 12b. The microstructure exhibits columnar grains with a number of isolated smaller coaxial grains.

A bright field TEM micrograph from the actuated sample is presented in Fig. 12c along with a diffraction pattern insert that shows the diffraction condition. Columnar grains are observed in the image. These are about 200 nm in width. Smaller grains are also observed in the central regions at the top of the image. Furthermore, the columnar grains are oriented towards the growth direction (Fig. 12c). However, a misorientation angle is observed between the columnar grains.

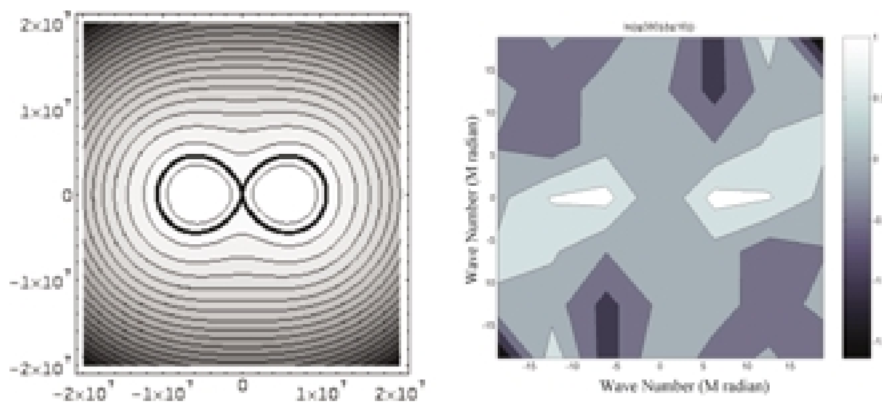

Figure 10 (a) Contours of α corresponding to the stress at the notch tip and (b) Contours of $\ln \frac{q(w,t)}{q(w,0)}$ corresponding to an area of 2 μm × 2 μm near the notch tip.

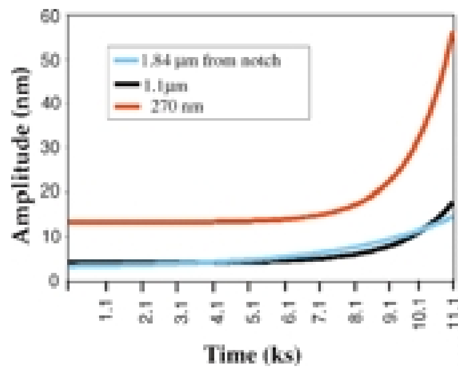

Figure 11 Groove amplitude as a function of actuation time. The curves are fitted to the actual data and represent areas close and far away from the notch root.

4.5. Fracture modes

Three-dimensional images of surface (before and after fracture) are shown in Fig. 13. There are two grooves marked by arrows in Fig. 13a. As seen from the side of the notch, the grooves run deep into the bulk of the sample. Comparing these grooves with the fracture planes of the sample in Fig. 13b, it is clear that fracture was initiated at the sites of these grooves. This clearly demonstrates the initiation of cracks from deep grooves on the surface of the sample.

To study the interaction of cracks with the microstructure, including single crystal silicon substrate, polysilicon layers, and topmost silica layer indentation test was carried out on a location at the vicinity of the notch. Fig. 13c–d are SE images from the indentation area at low and high magnifications. Fig. 13c illustrates the crack emanated from the indent into the top silica layer used for sealing the structure for fabrication and transference into the polysilicon layer underneath. It is clear that bridging can take place in these structures as labeled in Fig. 13c (with an arrow). The crack path is also transgranular is this figure.

Termination of the crack is illustrated in Fig. 13d. As marked with an arrow, the crack tip is located within a polysilicon grain. Crack interaction with multiple layers of the resonant structure is shown in Fig. 13e. A single crack is labeled with three arrows. The crack initiates in the topical silica layer, transfers to the top polysilicon 2, continues into polysilicon 1, and eventually crosses into the single crystal silicon substrate underneath without significantly changing its direction at the interfaces. The chipping of the top polysilicon layers shows that cracks can initiate in the silicon substrate and then propagate at or near the silicon/polysilicon interface. These cracks are seen to change their plane, cross the polysilicon layers and terminate at the surface.

4.6. Implications

The susceptibility of silicon microcomponents to cyclic fatigue has been attributed recently to sequential oxidation and stress corrosion cracking of the native oxide layer [27]. High voltage transmission electron microscopy has also shown that thickening of the topical SiO_2 layer during actuation of the structures [16]. The observed thickening is consistent with the current surface topography measurements that indicate the RMS surface roughness values (20–80 nm). Such surface roughnesses are much larger than the initial SiO_2 thickness values of (2–4 nm) [28]. They can only occur if

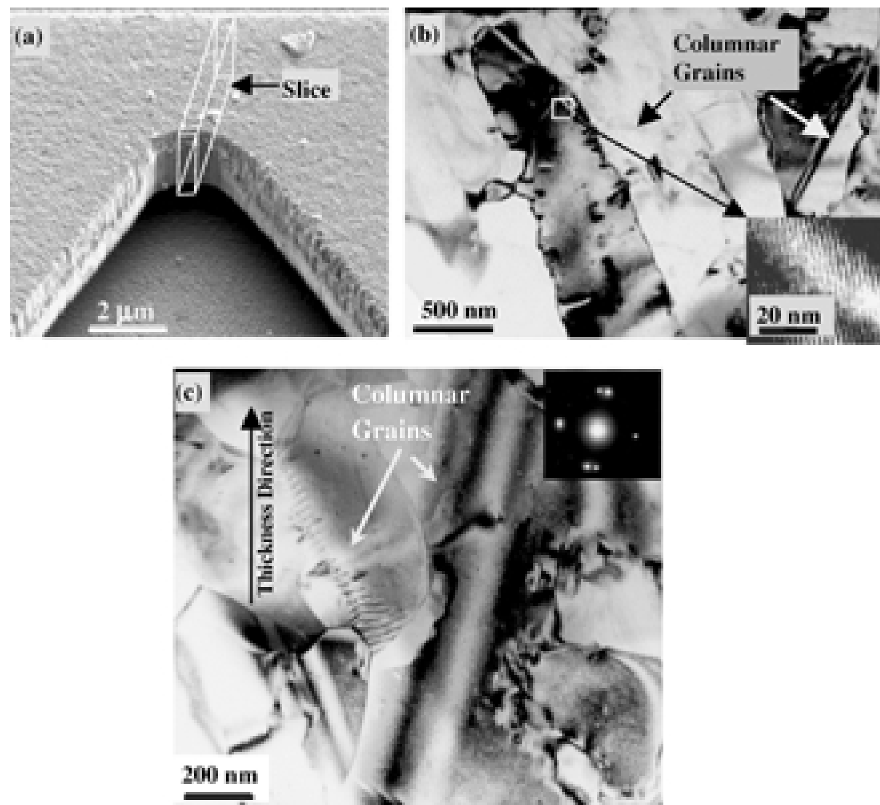

Figure 12 Notch tip TEM of: (a) Location of the TEM slice on the cantilever, (b) unactuated sample, and (c) actuated sample.

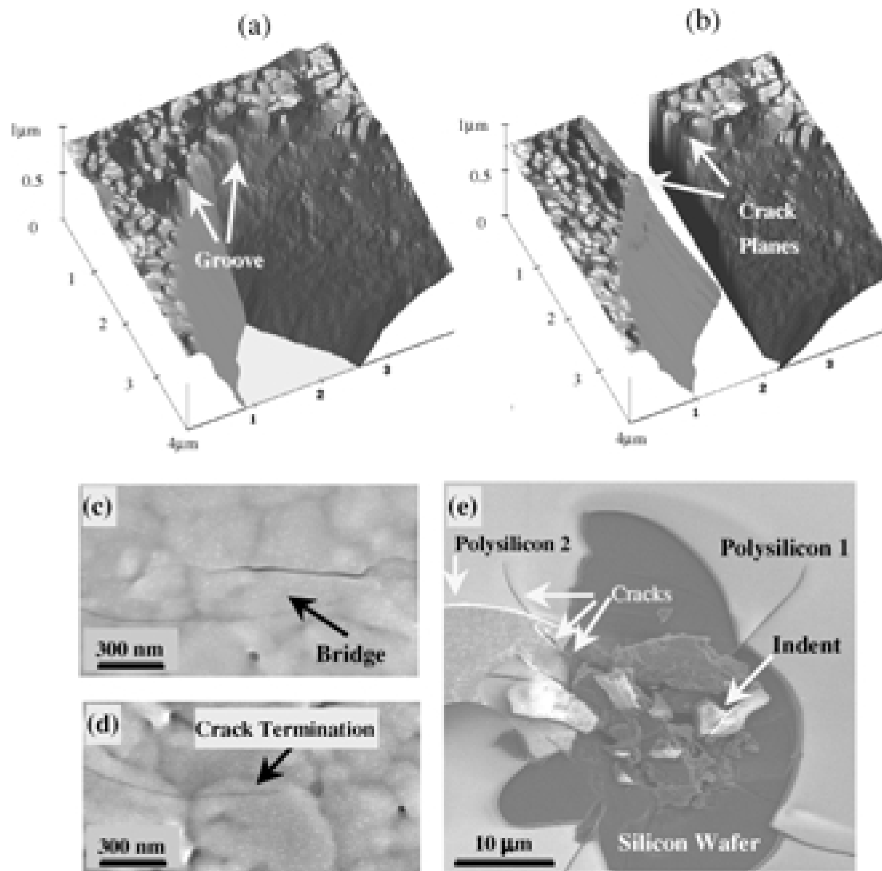

Figure 13 Polysilicon structure (a) before and (b) after fracture. (c) Crack emanated from an indent, (d) Crack termination inside a grain, (e) Various layers of the Si structure.

the surface oxides thicken to levels that are at least consistent with maximum groove depths.

Fig. 5 demonstrates the effect of stress on the surface topography evolution of polysilicon structures. The observed phenomena are consistent with a mechanism based on stress-assisted dissolution of silica layer. The roughening of the topical oxide layer can be attributed to dissolution of the SiO_2 layer in the areas that experience highest stress levels. However, reasons for the oxide thickening are not fully understood at present. Deepening of surface grooves in the areas of high stresses was demonstrated in Fig. 9. Such deepening can lead to the sharp grooves that can ultimately evolve into cracks. However, the precise transition from micro-grooves into micro-cracks is yet to be shown in the experiments. Nevertheless, recent work by Muhlstein *et al*. (2001) has shown that micro-cracks form in the topical SiO_2 layer after fatigue cycling of the same type of inter-digitating Si MEMS structures.

Further work by Muhlstein *et al.* (2001) [16, 17] has also demonstrated the thickening of the surface oxide during cyclic actuation of Si MEMS structures. The authors concluded that the change in the resonant frequency of the resonant structure (during cyclic actuation) could be representative of crack growth in the native oxide layer, which thickens with time. The critical crack length was reported to be less than 66 nm for over 20 samples tested. The whole length of the critical crack at fracture then will be located in the native oxide layer, which was reported to be 100 nm. While the decrease in the resonant frequency may well be due to cracking of the native oxide layer, surface morphological changes at the crack root area and damping effects can also contribute to drops in the resonant frequency.

The thickening of the native oxide layer at the notch root observed by Muhlstein *et al*. [16, 17] was related to the presence of moisture in the laboratory air and also to the presence of highest levels of stress in that region. Similar conditions exist on the top surface of the cantilever (in close vicinity of the notch) examined in this study. Also, since the magnitude of surface morphological changes observed in these experiments do not exceed 100 nm, the entire change in the topography are, therefore, in the topical oxide layer.

Surface morphology evolution, therefore, initiates in the SiO_2 layer where the stresses are over 2 GPa in the vicinity of the notch root up to a distance of 250 nm, and over 1 GPa up to 1 μm away from the notch (Fig. 8). Under these conditions, it is not unreasonable to assume there will develop a native oxide layer on the surface of the specimen that would taper off as it grows away from the notch root. This is consistent with the gradient observed in the surface morphological changes (upon cyclic actuation), as shown in Fig. 5.

Based on the results of this work and others [5, 15, 16, 29], it is possible to postulate the following micromechanisms operative in the nucleation and propagation of cracks in resonant structures undergoing cyclic fatigue: The formation of a native oxide that thickens with cyclic actuation of resonant structures in the areas with a high stress (GPa range); Subsequent dissolution of this layer that leads to the surface topography evolution, crack

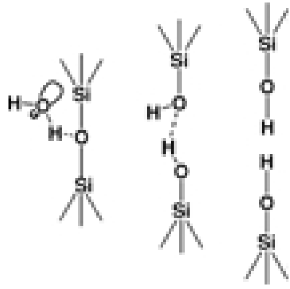

Figure 14 Migration of water molecules, in stressed silica, to strained bonds at the notch root.

nucleation and crack growth, and then final fracture. The details of the dissolution and morphology evolution will be discussed here.

Dissolution rate of silica in water at room temperature is ∼10 nm/year [28]. Possible Dissolution mechanisms include hydration, hydrolysis and ionic exchanges [28] of which the latter is not applicable here. Dominant reactions between water and silica involve silanol group formation (≡Si—OH). In addition to the formation of silanol, the hydroxylation of siloxane results in the break up of the structural backbone of SiO_2. Water adheres primarily by the hydrogen bonds to hydrated surfaces (Fig. 14).

For the stressed silica, water molecules migrate to strained bonds such as those at crack or notch tips [30]. Subsequent reactions result in the reconfiguration of the siloxane bond into two hydroxyl-terminated groups. The loosely connected hydroxyl-terminated groups are then connected by weak hydrogen bonds. The strained bond state results from the reconfiguration of the water molecule and Si atom orbital. According to Shreter *et al.* [31] stressed silicon develops crack-like defects in echants under compression. This might partly explain the increased susceptibility of silicon to compression fatigue, when compared to its resistance to tension fatigue [32].

A non-linear analysis of temporal evolution of the surface morphology of a stressed solid was formulated by Yang and Srolovitz [19], who proposed that the surfaces of elastic, defect free solids are unstable against the nucleation and growth of cracks. Surface instability creates a groove that sharpens, as it grows deeper. This stress-assisted dissolution is formulated differently by Liang and Suo [20] relating the stress to the interfacial velocity, ν_s:

$$\nu_n = \nu_0 \exp\left(\frac{Q + S\varepsilon^*\Omega}{kT}\right) \quad (3)$$

Where S is stress of flat surface, ε^* is activation strain, and Ω is atomic volume. They postulate that stress not only affects the driving force for dissolution of silica, but also lowers the activation energy in Equation 1. The micromechanisms operative in the evolution of the surface morphology, therefore, consist of stress-assisted dissolution of the native silica layer, which thickens with time. The stress-assisted dissolution occurs at grooves, where they deepen and transform presumably into sharp cracks. Stress corrosion cracking then leads to the growth of these cracks, and eventual fast fracture from the topical SiO_2 layer, as shown by Muhlstein *et al.*, 2001 [16].

5. Summary and conlcuding remarks

1. *In situ* AFM observations of the surface topography of actuated polysilicon resonant notched structures show significant surface morphology changes. The extent of the surface topography evolution appears to increase with increasing stress level.

2. Quantitative analyses of topography changes that occur during actuation reveal an increase in the amplitude of larger wavelength perturbations in regions close to the notch root. Image subtraction on the images obtained from the same regions shows similar results.

3. The measured roughness values obtained after cyclic actuation are much greater than the initial surface oxide thickness levels of 2–4 nm. Since the roughening occurs in the topical SiO_2 layer, it is inferred that the surface oxide thickens upon cyclic actuation.

4. The linear perturbation analysis shows that the evolution of surface topography is associated with the stress-assisted dissolution of SiO_2.

5. The TEM analyses of cyclically deformed regions in the notch root regions show dislocation-like line defects. However, work is required to ascertain the extent to which these dislocation-like line defects contribute to notch-root deformation. Final fracture occurs by cleavage on planes with a high density of intersecting microgrooves.

References

1. A. D. ROMIG, "Opportunities and Challenges in MEMS Commercialization," *Vacuum Technology and Coating*, 2001.
2. M. MADOU, "Fundamentals of Microfabrication," 2nd ed. (CRC Press, New York, 2002).
3. W. M. MILLER, D. M. TANNER, S. L. SAMUEL and K. A. PETERSON, "MEMS Reliability: The Challenge and the Promise," Presented in 4th Annual "The Reliability Challenge," 1998, Dublin, Ireland, p. 4.1.
4. P. T. JONES, G. C. JOHNSON and R. T. HOWE, "Fracture Strength of Polycrystalline Silicon," Presented in Microelectromechanical Structures for Materials Research-Symposium N (Materials Research Society, 1998) p. 197.
5. S. B. BROWN, W. V. ARSDELL and C. L. MUHLSTEIN, "Materials Reliability in MEMS Devices," Presented in Transducers 97, International Conference on Solid-State Sensors and Actuators, Digest of Technical Papers, 1997, Chicago, IL, edited by S. Senturia, p. 591.
6. D. LAVAN and T. E. BUCHHEIT, "Testing of Critical Features of Polysilicon MEMS," Presented in Symposium MM, Materials Science of Microelectromechanical Systems (MEMS) Devices II, (Materials Research Society, Boston, MA, 1999) p. 19.
7. H. KAHN, N. TAYEBI, R. L. BALLARINI, R. MULLEN and A. H. HEUER, "Fracture Toughness of Polysilicon MEMS Devices," Presented in 10th International Conference on Solid State Sensors and Actuators (Transducers '99), 1999, Sendai, Japan, p. 274.
8. C. P. CHEN and M. H. LEIPOLD, *Amer. Ceram. Soc. Bull.* **59** (1980) 469.
9. R. L. BALLARINI, R. MULLEN, Y. YIN, H. KAHN, S. STEMMER and A. H. HEUER, *Adv. Appl. Mech.* **12** (1997) 915.
10. B. WONG and R. J. HOLBROOK, *J. Electrochem. Soc.* **134** (1987) 2254.
11. C. ST. JOHN, *Phil. Mag.* (1975) 1193.
12. R. O. RITCHIE, *Int. J. Fract.* **100** (1999) 55.

13. S. SURESH, "Fatigue of Materials," 2nd ed. (Cambridge University Press, 1998).
14. H. KAPELS, R. AIGNER and J. BIDER, "Fracture Strength and Fatigue of Polysilicon Determined by A Novel Thermal Actuator [MEMS]," Presented in 29th European Solid-State Device Research Conference, 1999, Leuven, Belgium, p. 1522.
15. C. L. MUHLSTEIN, S. BROWN and R. O. RITCHIE, "High Cycle Fatigue of Polycrystalline Silicon Thin Films in Laboratory Air," Presented in Materials Science of Microelectromechanical System (MEMS) Devices III, 2000, Boston, MA, edited by H. Kahn, et al., p. EE5.8.1.
16. C. L. MUHLSTEIN, E. A. STACH and R. O. RITCHIE, *Acta Met. et. Mater.* 2001, Submitted.
17. *Idem.*, *Appl. Phys. Let.*, 2001, In Press.
18. S. M. ALLAMEH, B. GALLY, S. BROWN and W. O. SOBOYEJO (eds.) "Surface Topology and Fatigue in Si MEMS Structures," Mechanical Properties of Structural Films, edited by C. L. Muhlstein and S. Brown, Vol. STP 1413 (American Society for Testing and Materials West Conshohocken, PA, 2001) p. 3.
19. W. H. YANG and D. J. SROLOVITZ, *J. Mech. Phys. Solids*, **42**(10) (1994) 1551.
20. J. LIANG and Z. SUO, *Interf. Sci.* **9**(1–2) (2001) 93.
21. P. SHROTRIYA, S. M. ALLAMEH and W. O. SOBOYEJO, "On the Evolution of Surface Morphology of Polysilicon MEMS Structures During Fatigue," Presented in Annual Meeting of ASME, 2001, New York, NY, edited by R. Ballarini, S. M. Allameh and W. O. Soboyejo, In Press.
22. W. N. SHARPE, "Variation in Mechanical Properties of Polysilicon," Presented in 43rd International Symposium of Instrumentation Society of America, 1997, Orlando, FL, p. 179.
23. R. MULLINS, *J. Appl. Phys.* **28** (1957) 333.
24. D. J. SROLOVITZ, *Acta Met. et. Mater.* **37** (1989) 621.
25. H. H. YU and Z. SUO, *J. Appl. Phys.* **87** (2000) 1211.
26. K.-S. KIM, J. A. HURTADO and H. TAN, *Phys. Rev. Lett.* **83**(19) (1999) 3872.
27. C. L. MUHLSTEIN, R. T. HOWE and R. O. RITCHIE, *Mech. Mater.* (2002) Submitted.
28. B. C. BUNKER, *J. Nanocrystall. Solids* **179** (1994) 300.
29. S. B. BROWN, S. POVUK and J. A. CONNALLY, "Measurement of Slow Crack Growth in Silicon and Nickel Micromechanical Devices," Presented in MEMS-93, 1993, fort Lauderdale, FL, p. 99.
30. S. W. FREIMAN, G. S. WHITE and E. R. FULLER, JR., *J. Amer. Ceram. Soc.* **68** (1985) 108.
31. Y. G. SHRETER, D. V. TARKHIN, S. A. KHOREV and Y. T. REBANE, *Phys. Solid State* **41**(8) (1999) 1295.
32. R. L. BALLARINI, H. KAHN and A. H. HEUER, 2002, Unplublished work.